

The spatial distributions of chiral magnetic field in the RHIC and LHC energy regions

Yang Zhong^{1,2}, Chun-Bin Yang^{1,3}, Xu Cai^{1,3}, and Sheng-Qin Feng^{2,3}

¹ *Institute of Particle Physics, Central China Normal University, Wuhan 430079, China*

² *Department of Physics, College of Science, China Three Gorges University, Yichang 443002, China and*

³ *Key Laboratory of Quark and Lepton Physics (MOE),
Central China Normal University, Wuhan 430079, China*

Relativistic heavy-ion collisions can produce extremely strong magnetic field in the collision regions. The spatial variation features of the magnetic fields are analyzed in detail for non-central Pb - Pb collisions at LHC $\sqrt{s_{NN}} = 900, 2760$ and 7000 GeV and Au-Au collisions at RHIC $\sqrt{s_{NN}} = 62.4, 130$ and 200 GeV. The dependencies of magnetic field on proper time, collision energies and impact parameters are investigated in this paper. It is shown that a enormous with highly inhomogeneous spatial distribution magnetic field can indeed be created in off-central relativistic heavy-ion collisions in RHIC and LHC energy regions. The enormous magnetic field is quite large, especially just after the collision, and then decreases rapidly with time. We are surprised to find that the magnetic effect decreases with increasing energy from RHIC to LHC energy region. It is found that the magnitude of magnetic field in the LHC energy region is far less than that of magnetic field in the RHIC energy region.

Keywords: Spatial distribution of chiral magnetic field, Non-central collision, chiral magnetic field

PACS numbers: 25.75.Ld, 11.30.Er, 11.30.Rd

I. INTRODUCTION

The Chiral Magnetic Effect (CME) is the phenomenon of electric charge separation along the external magnetic field that is introduced by the chirality imbalance [1, 2]. It is proposed by Ref. [3–7] that off-central relativistic heavy-ion collisions can create strong transient magnetic fields due to the fast, oppositely directed motion of two colliding nuclei. The magnetic field perpendicular to the reaction plane is aligned. Extremely strong (electromagnetic) magnetic fields are present in non-central collisions, albeit for a very short time. Thus, relativistic heavy-ion collisions provide a unique terrestrial environment to study QCD in strong magnetic field surroundings [8–11]. This so-called chiral magnetic effect may serve as a sign of the local P and CP violation of QCD. By using relativistic heavy-ion collisions at the Relativistic Heavy-Ion Collider (RHIC) and the Large Hadron Collider (LHC), one can investigate the behavior of QCD at extremely high-energy densities.

In non-central collisions opposite charge quarks would tend to be emitted in opposite directions relative to the system angular momentum [9, 12–14]. This asymmetry in the emission of quarks would be reflected in an analogous asymmetry between positive- and negative-pion emission directions. This phenomenon is introduced by the large (electro-) magnetic field produced in non-central heavy-ion collisions. The same phenomenon can also be depicted in terms of induction of electric field by the (quasi) static magnetic field, which happens in the occurrence of these topologically nontrivial vacuum solutions. The induced electric field is parallel to the magnetic field and leads to the charge separation in that direction. Thus, the charge separation can be viewed as a nonzero electric dipole moment of the system.

Experimentally, RHIC [15–19] and LHC [20] have published the measurements of CME by the two-particle or three-particle correlations of charged particles with respect to the reaction plane, which are qualitatively consistent with the CME. A clear signal compatible with a charge dependent separation relative to the reaction plane is observed, which shows little or no collision energy dependence when compared to measurements at RHIC energies. This provides a new insight for understanding the nature of the charge-dependent azimuthal correlations observed at RHIC and LHC energies.

Recent years, lots of attentions [21–25] have been paid to the chiral magnetic effect (CME). It is shown that this effect originates from the existence of nontrivial topological configurations of gauge fields and their interplay with the chiral anomaly which results in an asymmetry between left- and right-handed quarks. The created strong magnetic field coupled to a chiral asymmetry can induce an electric charge current along the direction of a magnetic field. The strong magnetic field will separate particles of opposite charges with respect to the reaction plane. Recently, possible CME and topological charge fluctuations have been recognized by QCD lattice calculations in gauge theory [26, 27] and in QCD + QED with dynamical $2 + 1$ quark flavors [28]. Thus, such topological and CME effects in QCD might be recognized in relativistic heavy-ion collisions directly in the presence of very intense external electromagnetic fields.

Besides the chiral magnetic effect, there are other effects caused by the strong magnetic fields including the catalysis of chiral symmetry breaking [29], the spontaneous electromagnetic superconductivity of QCD vacuum [30, 31], the possible splitting of chiral and deconfinement phase transitions [32], the appearance of anisotropic viscosities [33–35], the possible enhancement

of elliptic flow of charged particles [35, 36], the emergence of the electric quadrupole moment of the QGP [37], the energy loss due to the synchrotron radiation of quarks [38], etc.

In Ref. [39, 40], we used the Wood-Saxon nucleon distribution instead of uniform distribution to improve the calculation of the magnetic field of the central point for non-central collision in the RHIC and LHC energy regions. In this paper, we will use the improved magnetic field model to calculate the spatial distribution feature of the chiral magnetic field in the RHIC and LHC energy regions. The dependencies of the spatial features of magnetic fields on the collision energies, centralities, and collision time will be systematically investigated, respectively.

The paper is organized as follows. The key points of the improved model of magnetic field are described in Sec. II. The calculation results of the magnetic field are present in Sec. III. A summary is given in Sec. IV.

II. THE IMPROVED MODEL OF CHIRAL MAGNETIC FIELD

The improved model of magnetic field mainly contains three parts:

(1) As shown in Fig.1, two similar relativistic heavy nuclei with charge Z and radius R are traveling in the positive and negative z direction with rapidity Y_0 . At $t = 0$ they go through a non-central collision with impact parameter b at the origin point. The center of the two nuclei are taken at $x = \pm b/2$ at time $t = 0$ so that the direction of b lies along the x axis. The region in which the two nuclei overlap contains the participants, the regions in which they do not overlap contain the spectators.

As the nuclei are nearly traveling with the speed of light in ultra-relativistic heavy-ion collision experiments, the Lorentz contraction factor γ is so large that the two included nuclei can be taken as pancake shape (as the $z = 0$ plane). We use the Wood-Saxon nuclear distribution instead of uniform nuclear distribution [1]. The Wood-Saxon nuclear distribution forms is:

$$n_A(r) = \frac{n_0}{1 + \exp\left(\frac{r-R}{d}\right)}, \quad (1)$$

here $d = 0.54$ fm, $n_0 = 0.17$ fm $^{-3}$ and the radius $R = 1.12$ A $^{1/3}$ fm. Considering the Lorentz contraction, the density of the two-dimensional plane can be given by:

$$\rho_{\pm}(\vec{x}'_{\perp}) = N \cdot \int_{-\infty}^{\infty} dz' \frac{n_0}{1 + \exp\left(\frac{\sqrt{(x' \mp b/2)^2 + y'^2 + z'^2} - R}{d}\right)}, \quad (2)$$

where N is the normalization constant. The number densities of the colliding nuclei can be normalized as

$$\int d\vec{x}'_{\perp} \rho_{\pm}(\vec{x}'_{\perp}) = 1. \quad (3)$$

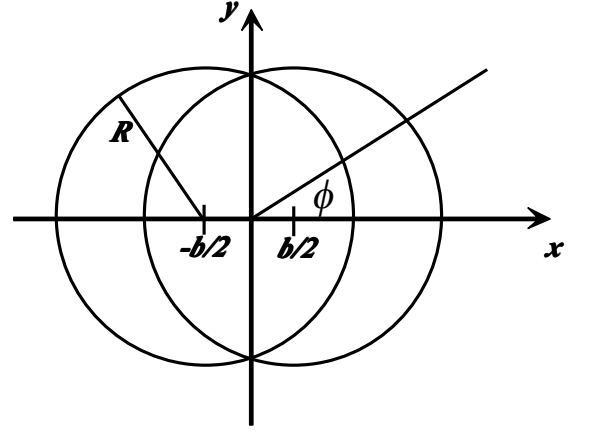


FIG. 1: Cross-sectional view of a non-central relativistic heavy-ion collision along the z axis. The two nuclei have same radii R , move in opposite directions, and collide with impact parameter b . The angle ϕ is an azimuthal angle with respect to the reaction plane. The plane $y = 0$ is called the reaction plane. The two nuclei overlap region contains the participants, and they do not overlap regions contain the spectators.

(2) Secondly, in order to study the strength of the magnetic field caused by the two relativistic traveling nuclei, we can split the contribution of particles to the magnetic field in the time $t > 0$. The specific forms of expression for the contribution of particles to the magnetic field in the following way

$$\vec{B} = \vec{B}_s^+ + \vec{B}_s^- + \vec{B}_p^+ + \vec{B}_p^- \quad (4)$$

where \vec{B}_s^{\pm} and \vec{B}_p^{\pm} are the contributions of the spectators and the participants moving in the positive or negative z direction, respectively. For spectators, we assume that they do not scatter at all and that they keep traveling with the beam rapidity Y_0 . Combining with Eq.(2), we use the density above and give

$$e\vec{B}_s^{\pm}(\tau, \eta, \vec{x}_{\perp}) = \pm Z\alpha_{EM} \sinh(Y_0 \mp \eta) \int d^2\vec{x}'_{\perp} \rho_{\pm}(\vec{x}'_{\perp}) \times [1 - \theta_{\mp}(\vec{x}'_{\perp})] \frac{(\vec{x}'_{\perp} - \vec{x}_{\perp}) \times \vec{e}_z}{[(\vec{x}'_{\perp} - \vec{x}_{\perp})^2 + \tau^2 \sinh(Y_0 \mp \eta)^2]^{3/2}} \quad (5)$$

where $\tau = (t^2 - z^2)^{1/2}$ is the proper time, $\eta = \frac{1}{2} \ln[(t+z)/(t-z)]$ is the space-time rapidity, and

$$\theta_{\mp}(\vec{x}'_{\perp}) = \theta[R^2 - (\vec{x}'_{\perp} \pm \vec{b}/2)^2]. \quad (6)$$

In the other hand, the distribution of participants that remain traveling along the beam axis is given by

$$f(Y) = \frac{a}{2 \sinh(aY_0)} e^{aY}, \quad -Y_0 \leq Y \leq Y_0. \quad (7)$$

Experimental data gives $a \approx 1/2$, which is consistent with the baryon junction stopping mechanism. The contribution of the participants to the magnetic field can be given by

$$e\vec{B}_p^\pm(\tau, \eta, \vec{x}_\perp) = \pm Z\alpha_{EM} \int d^2\vec{x}'_\perp \int dY f(Y) \sinh(Y \mp \eta) \times \rho_\pm(\vec{x}'_\perp) \theta_\mp(\vec{x}'_\perp) \frac{(\vec{x}'_\perp - \vec{x}_\perp) \times \vec{e}_z}{[(\vec{x}'_\perp - \vec{x}_\perp)^2 + \tau^2 \sinh(Y \mp \eta)^2]^{\frac{3}{2}}} \quad (8)$$

(3) In the third part, in order to study the spatial distribution of the magnetic field, we will calculate the eB_x and eB_y components of the chiral magnetic field from spectator and participant nuclei. The specific forms of the contribution of eB_x and eB_y components from the spectator and participant nuclei are given as follows:

$$eB_{sy}^\pm(\tau, \eta, \vec{x}_\perp) = \mp Z\alpha_{EM} \sinh(Y_0 \mp \eta) \int d^2\vec{x}'_\perp \rho_\pm(\vec{x}'_\perp) \times [1 - \theta_\mp(\vec{x}'_\perp)] \frac{(x' - x)}{[(\vec{x}'_\perp - \vec{x}_\perp)^2 + \tau^2 \sinh(Y_0 \mp \eta)^2]^{3/2}} \quad (9)$$

where eB_{sy} is the y component of magnetic field from spectators, and the x component of magnetic field from spectators is given by:

$$eB_{sx}^\pm(\tau, \eta, \vec{x}_\perp) = \pm Z\alpha_{EM} \sinh(Y_0 \mp \eta) \int d^2\vec{x}'_\perp \rho_\pm(\vec{x}'_\perp) \times [1 - \theta_\mp(\vec{x}'_\perp)] \frac{(y' - y)}{[(\vec{x}'_\perp - \vec{x}_\perp)^2 + \tau^2 \sinh(Y_0 \mp \eta)^2]^{3/2}} \quad (10)$$

In the other hand, the y component of magnetic field from participants is given by:

$$eB_{py}^\pm(\tau, \eta, \vec{x}_\perp) = \mp Z\alpha_{EM} \int d^2\vec{x}'_\perp \int dY f(Y) \sinh(Y \mp \eta) \times \rho_\pm(\vec{x}'_\perp) \theta_\mp(\vec{x}'_\perp) \frac{(x' - x)}{[(\vec{x}'_\perp - \vec{x}_\perp)^2 + \tau^2 \sinh(Y \mp \eta)^2]^{\frac{3}{2}}} \quad (11)$$

and the x component of magnetic field from participants is given by:

$$eB_{px}^\pm(\tau, \eta, \vec{x}_\perp) = \pm Z\alpha_{EM} \int d^2\vec{x}'_\perp \int dY f(Y) \sinh(Y \mp \eta) \times \rho_\pm(\vec{x}'_\perp) \theta_\mp(\vec{x}'_\perp) \frac{(y' - y)}{[(\vec{x}'_\perp - \vec{x}_\perp)^2 + \tau^2 \sinh(Y \mp \eta)^2]^{\frac{3}{2}}} \quad (12)$$

III. THE CALCULATION RESULTS

A. The energy relation

For consistency with the experimental results, we take Au-Au collision with RHIC energy region and Pb-Pb collision with LHC energy region. When studying the spatial distribution characteristics of magnetic field, we

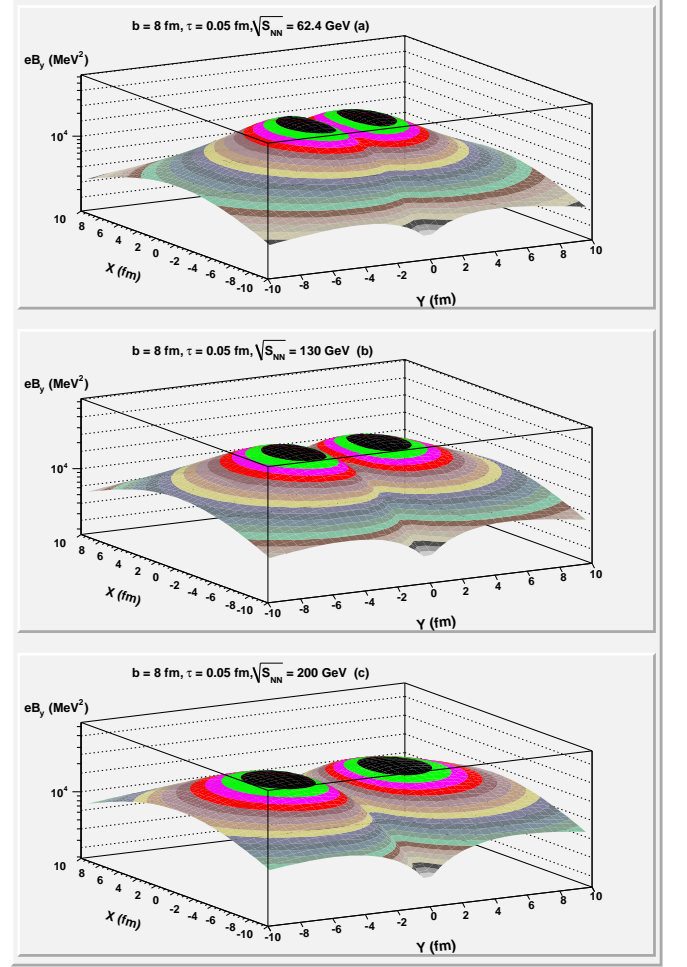


FIG. 2: The dependencies of magnetic field spatial distributions of eB_y on different collision energies $\sqrt{s_{NN}} = 62.4$ GeV(a), 130 GeV(b) and 200 GeV(c), respectively. The impact parameters $b = 8$ fm and proper times $\tau = 0.05$ fm.

choose the spatial regions of $-10.0 \text{ fm} \leq x \leq 10.0 \text{ fm}$ and $-10.0 \text{ fm} \leq y \leq 10.0 \text{ fm}$.

Figure 2 shows the magnetic field spatial distributions of eB_y with different collision energies $\sqrt{s_{NN}} = 62.4$ GeV, 130 GeV and 200 GeV. The collision energies shown in Fig.2 are in RHIC energy region. The spatial distributions of eB_y show obviously axis symmetry characteristics along $x = 0$ and $y = 0$ axes. On both sides of $y = 0$ line, there are two symmetrical peaks. These two peaks are almost connected when $\sqrt{s_{NN}} = 62.4$ GeV. As the collision energy increases, the two peaks start to separate and expose the valley between the two peaks when $\sqrt{s_{NN}} = 130$ GeV and 200 GeV. The maximum of magnetic field eB_y in RHIC energy region reaches $1.2 \times 10^4 \text{ MeV}^2$.

Compared with Fig.2, Fig.3 shows the magnetic field spatial distributions of eB_y in the LHC energy region. When the collision energy rises up to 900 GeV in LHC

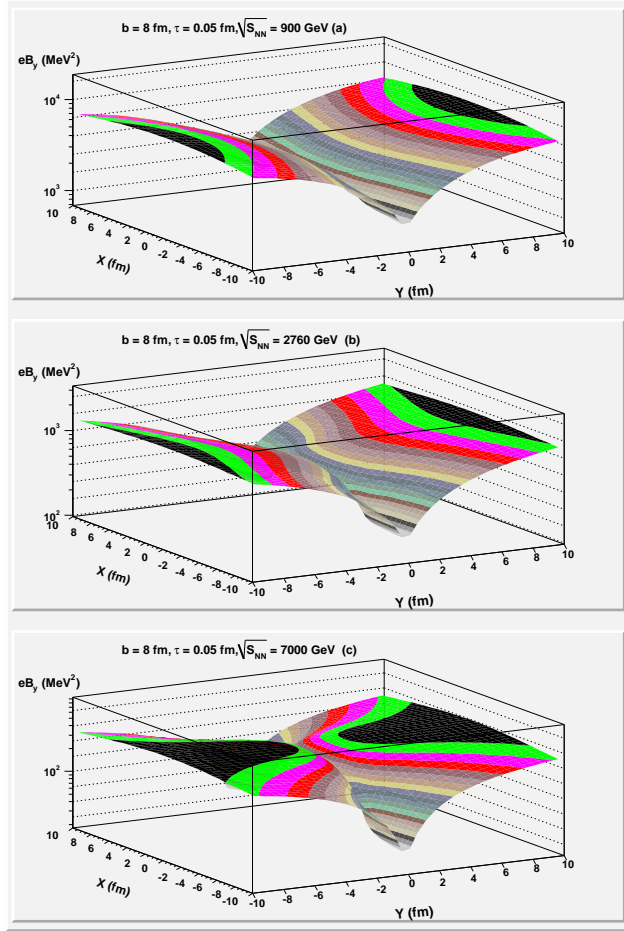


FIG. 3: The dependencies of magnetic field spatial distributions of eB_y on different collision energies $\sqrt{s_{NN}} = 900$ GeV(a), 2760 GeV(b), 7000 GeV(c), respectively. The impact parameters $b = 8$ fm and proper times $\tau = 0.05$ fm.

energy region, the distribution features of magnetic field are obviously different from that of the RHIC energy region. For example there are not peaks in the vicinity of $x = 0$ and $y = 0$. The valley of the spatial distributions of eB_y are located along $y = 0$, and the magnetic field begins to increase with y gradually away from the $y = 0$ line. The maximum of magnetic field eB_y in LHC energy region reaches 7.0×10^3 MeV², which is smaller than that of RHIC energy region.

The magnetic field spatial distributions of eB_x with different collision energies $\sqrt{s_{NN}} = 62.4$ GeV, 130 GeV and 200 GeV in the RHIC energy region are presented in Fig.4. It is shown that the magnetic field of eB_x is also highly inhomogeneous, has a minimum value along the $x = 0$ axis. The $x = 0$ is the symmetry axis and also the minimum. The magnetic field of eB_x begins to increase rapidly with x gradually away from the center position ($x = 0$). The maximum of magnetic field eB_x in RHIC energy region reaches 3.0×10^3 MeV².

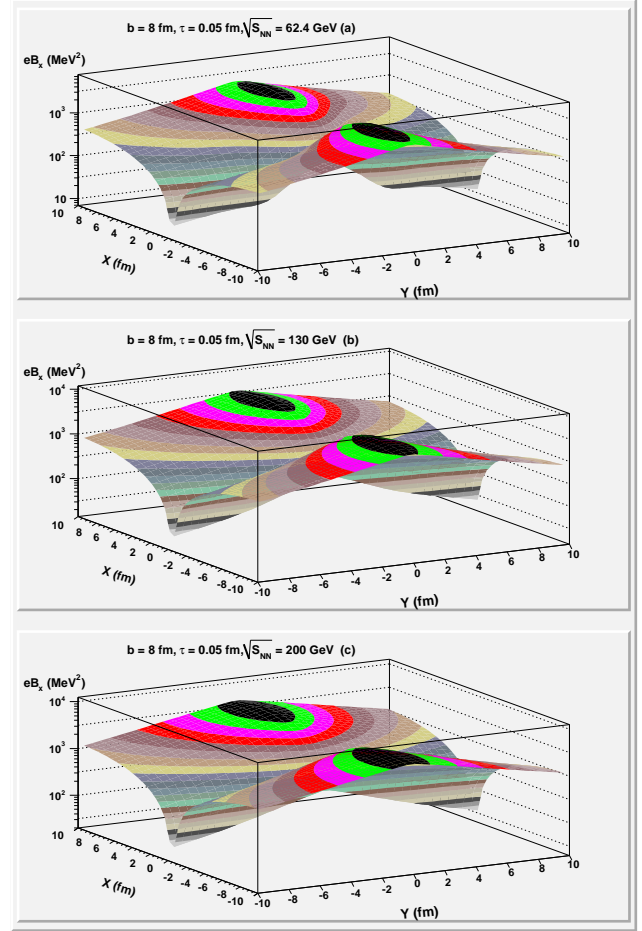


FIG. 4: The dependencies of magnetic field spatial distributions of eB_x on different collision energies $\sqrt{s_{NN}} = 62.4$ GeV(a), 130 GeV(b) and 200 GeV(c), respectively. The impact parameters $b = 8$ fm and proper times $\tau = 0.05$ fm.

Figure 5 shows the magnetic field spatial distributions of eB_x with different collision energies $\sqrt{s_{NN}} = 900$ GeV(a), 2760 GeV(b), 7000 GeV(c), respectively in the LHC energy region. The maximum of magnetic field eB_x in LHC energy region reaches 1.5×10^3 MeV² at $\sqrt{s_{NN}} = 900$ GeV. The magnetic field of eB_x begins to decrease rapidly with the collision energies increase. When $\sqrt{s_{NN}} = 7000$ GeV, the maximum of magnetic field eB_x is only about 50 MeV² which is far less than 1.5×10^3 MeV² at $\sqrt{s_{NN}} = 900$ GeV.

Figure 6 shows the dependencies of the magnetic field (eB_y and eB_x) on coordinate y at $\sqrt{s_{NN}} = 130$ GeV, 200 GeV, 2760 GeV and 7000 GeV, respectively in the LHC energy region. From Fig.6 we can find that the difference of eB_y or eB_x between $\sqrt{s_{NN}} = 130$ GeV and $\sqrt{s_{NN}} = 200$ GeV is very small, but the magnitudes of eB_y (or eB_x) distribution in the RHIC energy region are much larger than that of LHC energy region. Please also note that the curve shape of eB_y is different from that of

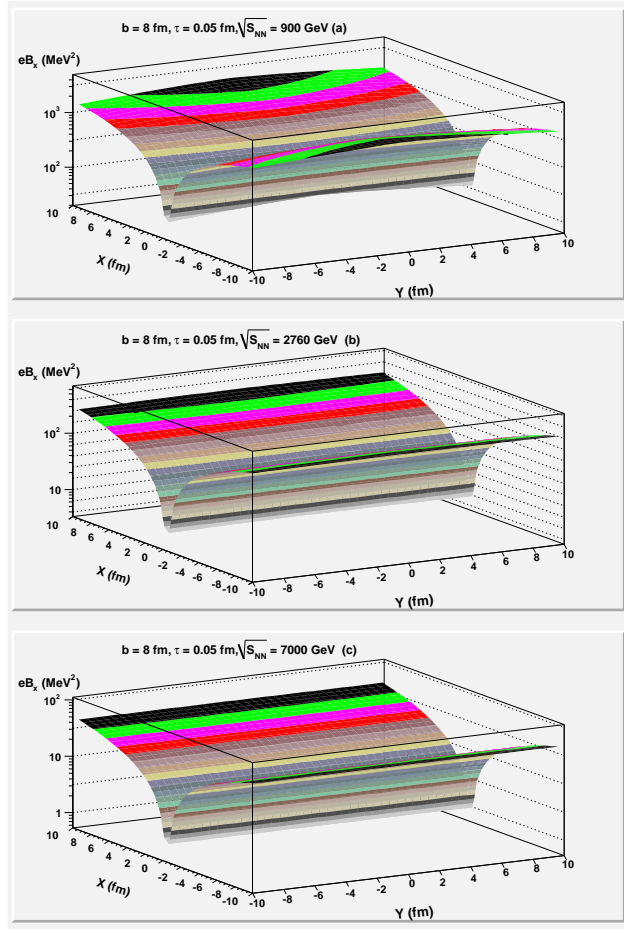


FIG. 5: The dependencies of magnetic field spatial distributions of eB_x on different collision energies $\sqrt{s_{NN}}=900$ GeV(a), 2760 GeV(b) and 7000 GeV(c), respectively. The impact parameters $b = 8$ fm and proper times $\tau = 0.05$ fm.

eB_x , the maximum of eB_y is located at $y = 0$, but the minimum of eB_x is located at $y = 0$.

Figure 7 shows the dependencies of the magnetic field (eB_y and eB_x) on x at $\sqrt{s_{NN}}=130$ GeV, 200 GeV, 2760 GeV and 7000 GeV, respectively. The magnitude of magnetic field on x at 200 GeV nearly equals to that of the magnitude of magnetic field at 130 GeV in the RHIC energy region. But the magnitudes of magnetic field in the RHIC are much larger than that of LHC energy region.

Figure 7 shows that eB_y has a dip locating at $x = 0$, and eB_y begins to decrease with collision energy increase. The eB_x is nearly zero at $y = 0$. The maximum of eB_x is located at $x = 0$ and then decrease with $|x|$ increase when $y = 5$ and 10 fm along with $\sqrt{s_{NN}} = 130$ GeV and 200 GeV. But for $\sqrt{s_{NN}} = 2760$ GeV and 7000 GeV, the magnitudes of eB_x are much more low and almost constant.

From Fig.2 to Fig.7, we argue that the magnetic field spatial distributions of eB_x and eB_y are highly inhomogeneous,

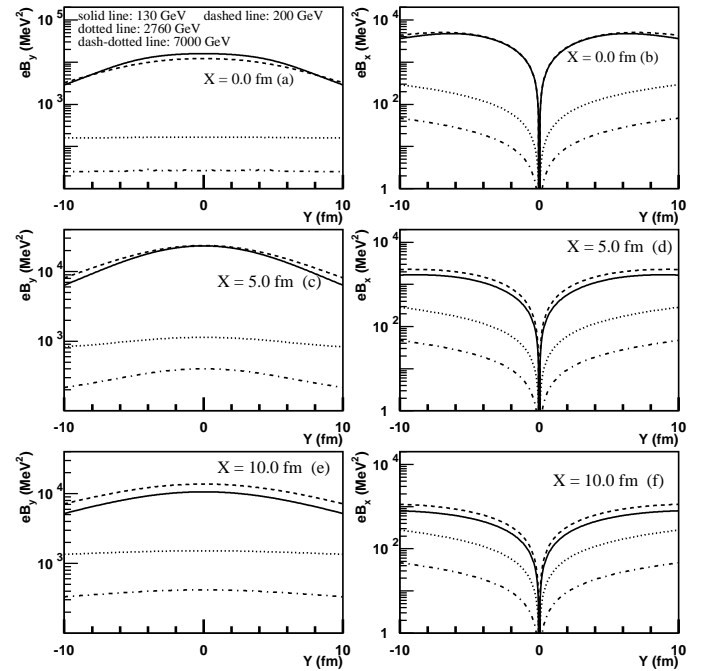


FIG. 6: The dependencies of the magnetic field (eB_y and eB_x) on y at different collision energies $\sqrt{s_{NN}}=130$ GeV, 200 GeV, 2760 GeV and 7000 GeV, respectively. The Fig.6(a, c and e) are for the relation of eB_y with y and Fig.6(b, d and f) are for the relation eB_x with y . Here $x = 0.0, 5.0$ and 10.0 fm, respectively.

and eB_x and eB_y distributions are completely different. The distribution features in the RHIC energy region is different from that of the LHC energy region. The magnitudes of magnetic field (eB_y and eB_x) change with the collision energy is not obvious in the RHIC energy region, but in the LHC energy region the magnitudes of eB_y and eB_x on collision energies decline sharply. Generally speaking, the magnitudes of magnetic field in the RHIC energy region are much larger than that of LHC energy region.

B. Impact parameter dependence

We calculate the spatial distributions of eB_y on impact parameters at $\sqrt{s_{NN}} = 2760$ GeV with Pb-Pb interactions in the LHC energy region. The lowest points are located on the line of $y = 0$, and the magnetic field begins to increase with the $|y|$ gradually increase. The three dimensional view are given in Fig.8.

The spatial distributions of eB_x on different impact parameters at $\sqrt{s_{NN}} = 2760$ GeV are shown in Fig.9. It is shown that the magnetic field spatial distribution characterizes of eB_x at $b = 4$ fm, $b = 8$ fm and $b = 12$ fm are nearly similar. Compared with eB_y distribution shown in Fig.8, the minimum of eB_x distribution are along the symmetrical axis $x = 0$. The magnetic field increases rapidly with the increase of $|x|$.

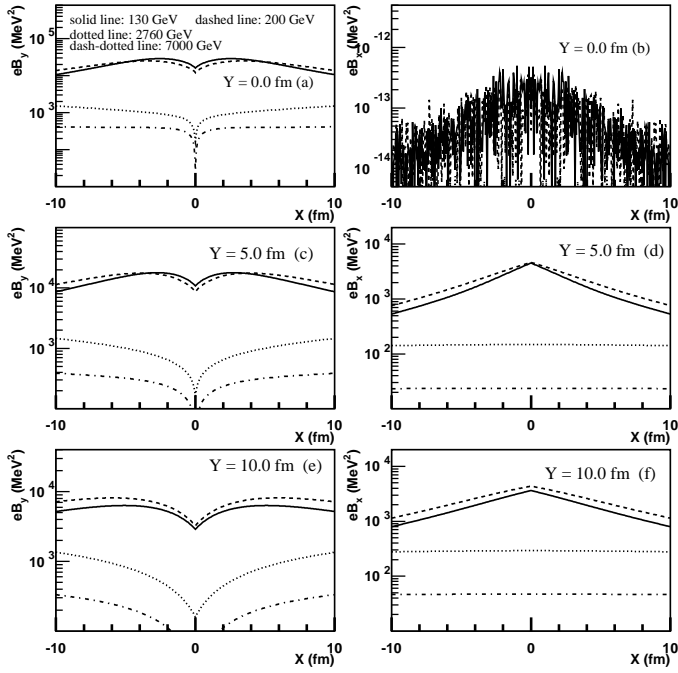


FIG. 7: The dependencies of the magnetic field (eB_y and eB_x) on x at different collision energies $\sqrt{s_{NN}} = 130$ GeV, 200 GeV, 2760 GeV and 7000 GeV, respectively. and at different coordinate y such as $y = 0.0$, 5.0 and 10 fm, respectively. The Fig.7(a, c and e) are for the relation of eB_y with x and Fig.7(b, d and f) are for the relation of eB_x with x . Here $y = 0.0$, 5.0 and 10 fm, respectively.

In order to study the detailed feature of magnetic field with impact parameter, we also discuss the dependencies of the magnetic field spatial distribution at different impact parameters $b = 4$ fm, $b = 8$ fm, $b = 12$ fm, respectively. Figure 10(a, c and e) shows that eB_y has a dip locating at $x = 0$, and eB_y begins to increase with $|x|$ increase. When $y = 0$, eB_x approaches zero. When $y \neq 0$, eB_x increases with the increase of b , but when b increases to 8, the growth rate slows down. So one can find that eB_x are nearly unchanged when $b = 8$ fm and $b = 12$ fm.

approaches zero. keeps nearly unchanged with x changes. The eB_x distributions are completely different from that of eB_y .

The dependencies of the magnetic field (eB_y and eB_x) on y at different impact parameters are presented in Fig.11. When $b = 4$ fm and $x = 0$, eB_y is nearly a value of zero with y changes. When $x \neq 0$, the peaks of eB_y distribution are located at $y = 0$. Compared with eB_y distribution, eB_x distribution is completely different. The minimum of the eB_x distribution is located at $y = 0$, and then eB_x increases linearly with the increase of $|y|$.

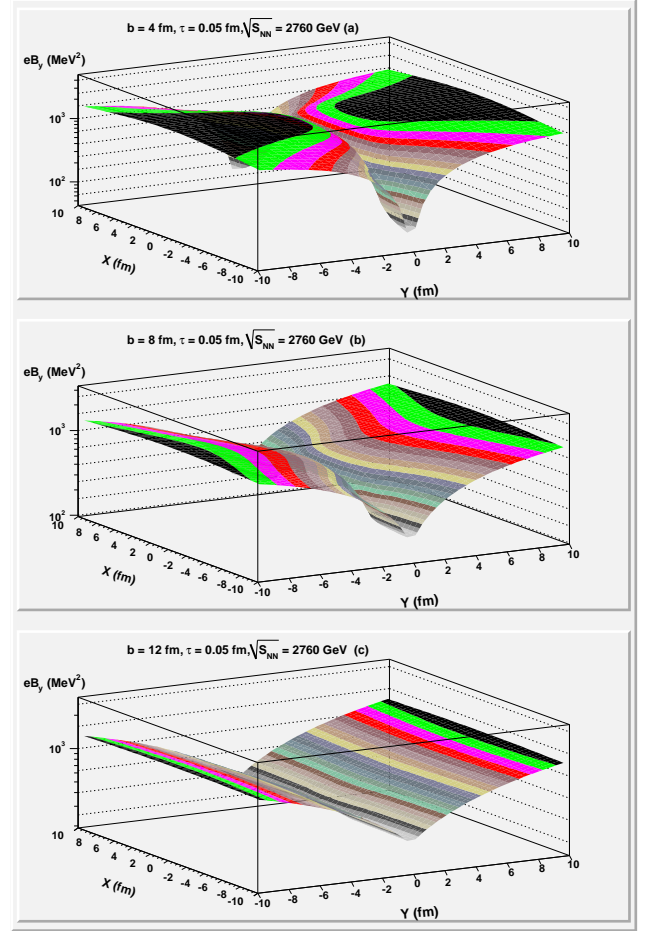


FIG. 8: The dependencies of magnetic field spatial distributions of eB_y on impact parameters $b = 4$ fm (a), $b = 8$ fm (b), $b = 12$ fm (c), respectively. The collision energy $\sqrt{s_{NN}} = 2760$ GeV and proper times $\tau = 0.05$ fm.

C. The proper time relation

The above we make a discussion of magnetic field spatial distributions with the collision energy and impact parameter relations, we will make a study of magnetic field with the proper time. Figure 12 presents the dependencies of the magnetic field eB spatial distributions of $\sqrt{s_{NN}} = 200$ GeV on the proper time $\tau = 0.02$, 0.2 and 2.0 fm, respectively. The magnitude of magnetic field is presented as:

$$eB = \sqrt{(eB_x)^2 + (eB_y)^2} \quad (13)$$

Figure 12 shows that when $\tau = 0.02$ fm, the maximum of the magnetic field can reaches 1.0×10^5 MeV², but when $\tau = 2$ fm, the maximum of the magnetic field is only about 0.9 MeV² at $\sqrt{s_{NN}} = 200$ GeV. We can argue that as time increases, the magnetic field decreases drastically in the RHIC energy region.

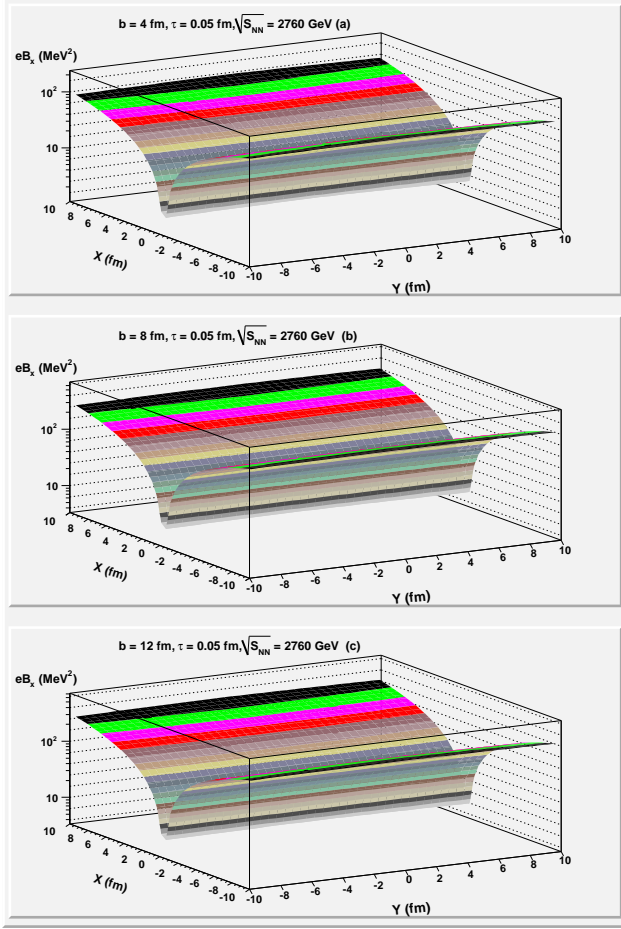


FIG. 9: The dependencies of magnetic field spatial distributions of eB_x on impact parameters $b = 4$ fm (a), $b = 8$ fm (b), $b = 12$ fm (c), respectively. The collision energy $\sqrt{s_{NN}} = 2760$ GeV and proper times $\tau = 0.05$ fm.

Figure 13 also shows the dependencies of the magnetic field spatial distribution eB at different proper time as shown in Fig.12, but for $\sqrt{s_{NN}} = 2760$ GeV. When $\tau = 0.02$ fm, the maximum of the magnetic field can reach 2.0×10^4 MeV² at $\sqrt{s_{NN}} = 2760$ GeV. But when $\tau = 2$ fm, the maximum of the magnetic field is only about 1.0 MeV² at $\sqrt{s_{NN}} = 2760$ GeV. It is also shown that as proper time increases, the magnetic field decreases drastically in the LHC energy region.

Sometimes, one often takes the y component eB_y to approximately replace eB . This is the reason that eB_y is usually larger than eB_x . In order to verify the rationality of the substitution, we need a detailed study the relation between eB_y and eB . Figure 14 shows the dependencies of the ratio of $eB_y/(eB)$ on x and y at $\sqrt{s_{NN}} = 200$ GeV and at different proper time $\tau = 0.02, 0.2$ and 2.0 fm, respectively. The Fig.14(a, c and e) are for $eB_y/(eB)$ with y at different proper time. From Fig.14(a, c and e), one can figure out that the ratio of $eB_y/(eB)$ with y

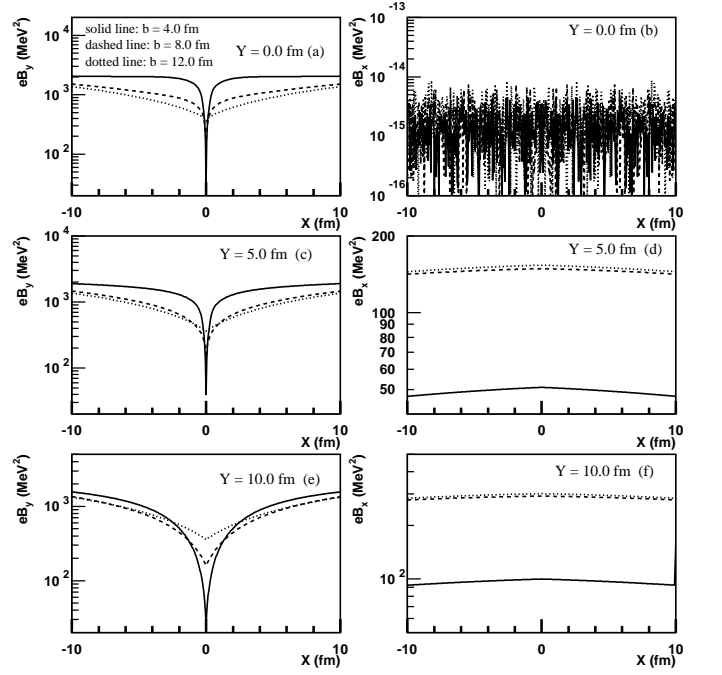


FIG. 10: The dependencies of the magnetic field(eB_y and eB_x) on coordinate x with proper times $\tau = 0.05$ fm, $\sqrt{s_{NN}} = 2760$ GeV and different impact parameters $b = 4$ fm, $b = 8$ fm, $b = 12$ fm, respectively. The Fig.10(a, c and e) are for eB_y with x and Fig.10(b, d and f) are for eB_x with x .

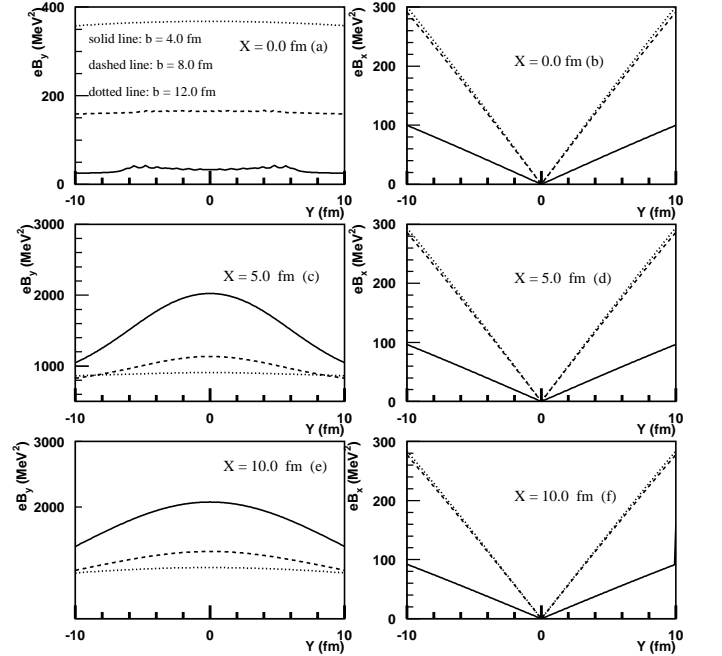


FIG. 11: The dependencies of the magnetic field(eB_y and eB_x) on coordinate y with proper times $\tau = 0.05$ fm, $\sqrt{s_{NN}} = 2760$ GeV and different impact parameters $b = 4$ fm, $b = 8$ fm, $b = 12$ fm, respectively. The Fig.11(a, c and e) are for eB_y with y and Fig.11(b, d and f) are for eB_x with y .

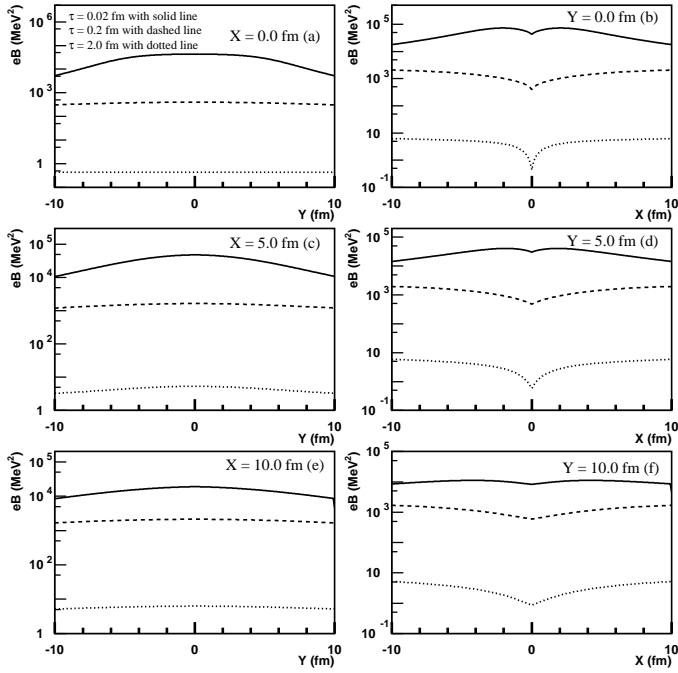


FIG. 12: The dependencies of the magnetic field spatial distribution eB on coordinate x and coordinate y at $\tau = 0.02, 0.2$ and 2.0 fm, respectively. Fig.12(a, c and e) are for eB with y and Fig.12(b, d and f) are for eB with x at different proper time. Here $\sqrt{s_{NN}} = 200$ GeV.

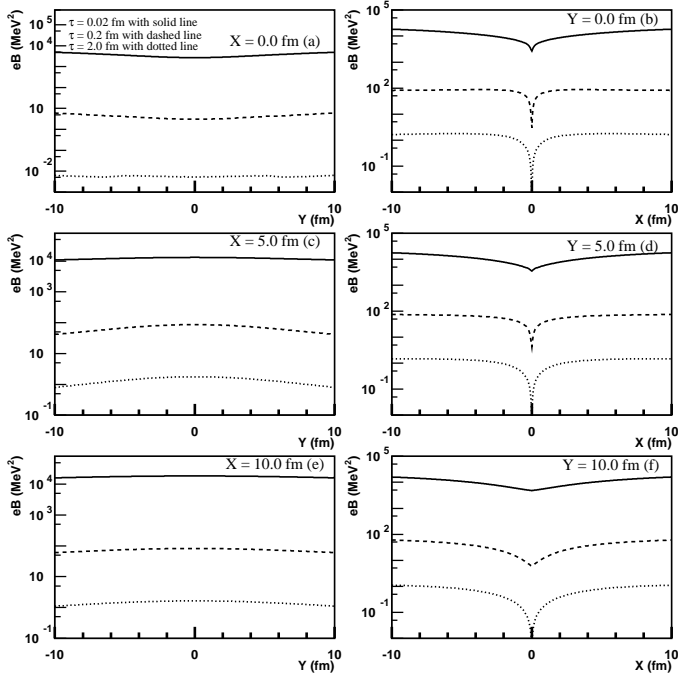


FIG. 13: The dependencies of the magnetic field spatial distribution eB on coordinate x and coordinate y at different proper time $\tau = 0.02, 0.2$ and 2.0 fm, respectively. Fig.13(a, c and e) are for eB with y and Fig.13(b, d and f) are for eB with x at different proper time. Here $\sqrt{s_{NN}} = 2760$ GeV.

change is between 0.9 to 1.0. In this case, one can approximate the eB_y instead of eB . Compared with the relation of ratio $eB_y/(eB)$ with y , the relationship of ratio $eB_y/(eB)$ with x shown as Fig.14(b, d and f) is obviously different. The main different is the dip located at $x = 0$. The minimum value of the ratio at $x = 0$ can be decreased to 0.5.

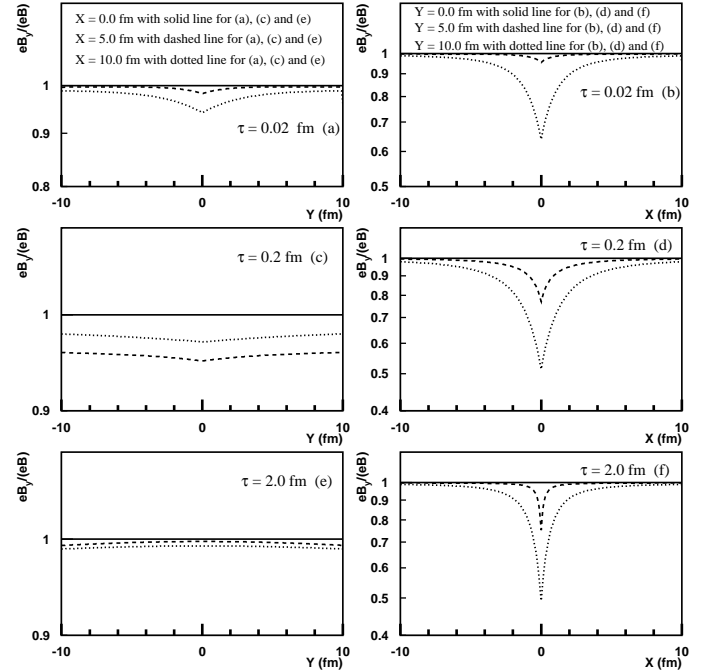


FIG. 14: The dependencies of the ratio of $eB_y/(eB)$ on x and y at $\sqrt{s_{NN}} = 200$ GeV and at different proper time $\tau = 0.02, 0.2$ and 2.0 fm, respectively. The Fig.14(a, c and e) are for $eB_y/(eB)$ with y and Fig.14(b, d and f) are for $eB_y/(eB)$ with x at different proper time.

When $\sqrt{s_{NN}} = 2760$ GeV, the ratios of $eB_y/(eB)$ approximately approach 1 in most case shown in Fig.15. But when $x = 0$, the ratio distribution is shown as a Gauss distribution, and the ratio variation region is between $0.5 \sim 1.0$.

IV. SUMMARY AND CONCLUSION

It is shown that an enormous magnetic field can indeed be created in off-central heavy-ion collisions. The magnetic field distributions of eB_x and eB_y are highly inhomogeneous, and eB_x and eB_y distributions are completely different. We were really surprised to find that the distribution features in the RHIC energy region is different from that of the LHC energy region, and then the magnitude of magnetic field decreases with the increase of collision energy in the LHC energy region. Generally speaking, the magnitude of magnetic field in LHC energy region is far less than that of RHIC energy region.

The dependencies of the ratio of $eB_y/(eB)$ on x and y at different collision energies at RHIC and LHC and at

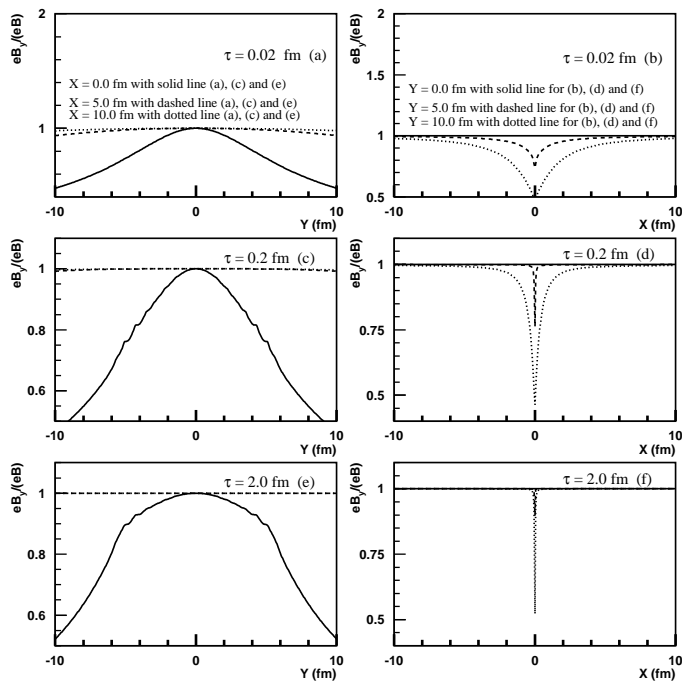


FIG. 15: The same dependencies of the ratio of $eB_y/(eB)$ on x and y as Fig.14 but for $\sqrt{s_{NN}}=2760$ GeV in the LHC energy region.

different proper time are analyzed in this paper. In most cases, the ratio $eB_y/(eB)$ approaches 1, so this is a good approximate by using eB_y to approximately replace eB . But one should note that the ratio $eB_y/(eB)$ is between $0.5 \sim 1.0$ along $x = 0$ line.

We systematically study the spatial distribution fea-

tures of chiral magnetic field in relativistic heavy-ion collisions at energies reached at LHC and RHIC with the improved model of chiral magnetic field in this paper. The feature of chiral magnetic fields at $\sqrt{s_{NN}}=900, 2760$ and 7000 GeV in the LHC energy region and $\sqrt{s_{NN}}=62.4, 130$ and 200 GeV in the RHIC energy region are systematically studied. The dependencies of the features of chiral magnetic fields on the collision CMS energies, centralities and collision proper time are systematically investigated, respectively.

The dependencies of the magnetic field on proper time and impact parameters for at RHIC and LHC energy regions, respectively. Comparing with that of RHIC energy region, one finds that the magnitudes of the magnetic fields with proper time fall more rapidly at LHC energy region. The variation characteristics of magnetic field with impact parameter at RHIC energy region are different from that of LHC energy region. The maximum position is located in the small proper time ($\tau \sim 0.02 fm$), more off-central collisions and $\sqrt{s_{NN}} \sim 200$ GeV. The maximum of magnetic field in our calculation is about $eB \simeq 10^5 MeV^2$ when $\tau = 0.02$, $b \simeq 8 fm$ and $\sqrt{s_{NN}} \sim 200$ GeV.

V. ACKNOWLEDGMENTS

This work was supported in part by National Natural Science Foundation of China (Grant No: 11375069, 1143505411075061, 10975091 and 11221504), by the Ministry of Education of China under Grant No. 306022, by the Programme of Introducing Talents of Discipline to Universities under Grant No. B08033 and Key Laboratory foundation of Quark and Lepton Physics (Central China Normal University)(QLPL2014P01).

-
- [1] D.E. Kharzeev, L.D. McLerran, H.J. Warringa, Nucl. Phys. A 803, 227 (2008). arXiv:0711.0950 [hep-ph].
 - [2] V. Skokov, A.Y. Illarionov, V. Toneev, Internat. J. Mod. Phys. A 24, 5925 (2009). arXiv:0907.1396 [nucl-th].
 - [3] K. Fukushima, D. E. Kharzeev, and H. J. Warringa, Phys. Rev. Lett. 104, 212001 (2010).
 - [4] W. T. Deng and X. G. Huang, Phys. Rev. C 85, 044907 (2012).
 - [5] K. Fukushima, D. E. Kharzeev, and H. J. Warringa, Nucl. Phys. A 836, 311 (2010).
 - [6] A. Bzdak and V. Skokov, Phys. Lett. B 710, 171 (2012)
 - [7] D. E. Kharzeev, Ann. Phys. (N.Y.) 325, 205 (2010).
 - [8] D. E. Kharzeev, D. T. Son, Phys. Rev. C 106, 062301 (2011).
 - [9] D. E. Kharzeev and A. Zhitnitsky, Nucl. Phys. A 797, 67 (2007).
 - [10] K. Fukushima, D. E. Kharzeev, and H. J. Warringa, Phys. Rev. D 78, 074033 (2008).
 - [11] Y. Burnier, D. E. Kharzeev, J. Liao and H.U. Yee, Phys. Rev. Lett. 107, 052303 (2011).
 - [12] D. Kharzeev, Phys. Lett. B 633, 260 (2006).
 - [13] S. Voloshin and Y. Zhang, Z. Phys. C 70, 665 (1996).
 - [14] S. A. Voloshin, Phys. Rev. C 70, 057901 (2004).
 - [15] B. I. Abelev, M. M. Aggarwal, Z. Ahammed et al., Phys. Rev. Lett. 103, 251601 (2009).
 - [16] B. I. Abelev, M. M. Aggarwal, Z. Ahammed et al., Phys. Rev. C 81, 054908 (2010).
 - [17] I. V. Selyuzhenkov and STAR Collaboration, Romanian Reports in Physics, 58, 49 (2006).
 - [18] S. A. Voloshin and STAR Collaboration, Nucl. Phys. A 830, 377 (2009).
 - [19] N. N. Ajitanand, R. A. Lacey, A. Taranenko, and J. M. Alexander et al., Phys. Rev. C 83, 011901 (2011).
 - [20] B. Abelev, J. Adam, D. Adamova et al., Phys. Rev. Lett. 110, 012301 (2009).
 - [21] D. Kharzeev, R. D. Pisarski, and M. N. G. Tytgat, Phys. Rev. Lett. 81, 512 (1998).
 - [22] D. Kharzeev, R. D. Pisarski, and M. N. G. Tytgat, Phys. Rev. D 61, 111901 (2000).
 - [23] D. Kharzeev, Phys. Lett. B 633, 260 (2006).
 - [24] K. Fukushima, M. Ruggieri, and R. Gatto, Phys. Rev. D 81, 114031 (2010);
 - [25] D. E. Kharzeev and H. J. Warringa, Phys. Rev. D 80, 034028 (2009).
 - [26] P. V. Buividovich, M. N. Chernodub, E. V. Luschevskaya, and M. I. Polikarpov, Phys. Rev. D

- 80, 054503 (2009)
- [27] P. V. Buividovich, M. N. Chernodub, E. V. Luschevskaya, and M. I. Polikarpov, Phys. Rev. D 81, 036007 (2010).
- [28] M. Abramczyk, T. Blum, G. Petropoulos, and R. Zhou, PoS (LAT2009) 181 (2009).
- [29] V. P. Gusynin, V. A. Miransky and I. A. Shovkovy, Phys. Rev. Lett. 73, 3499 (1994); 76, 1005(E) (1996).
- [30] M. N. Chernodub, Phys. Rev. D 82, 085011 (2010).
- [31] M. N. Chernodub, Phys. Rev. Lett. 106, 142003 (2011).
- [32] A. J. Mizher, M. N. Chernodub, and E. S. Fraga, Phys. Rev. D 82, 105016 (2010).
- [33] X. G. Huang, M. Huang, D. H. Rischke, and A. Sedrakian, Phys. Rev. D 81, 045015 (2010).
- [34] X. G. Huang, A. Sedrakian, and D. H. Rischke, Ann. Phys. (NY) 326, 3075 (2011).
- [35] K. Tuchin, J. Phys. G 39, 025010 (2012).
- [36] R. K. Mohapatra, P. S. Saumia, and A. M. Srivastava, Mod. Phys. Lett. A 26, 2477 (2011).
- [37] Y. Burnier, D. E. Kharzeev, J. Liao, and H. U. Yee, Phys. Rev. Lett. 107, 052303 (2011).
- [38] K. Tuchin, Phys. Rev. C 82, 034904 (2010); 83, 039903(E) (2011).
- [39] Y. J. Mo, S. Q. Feng and Y. F. Shi, Phys. Rev. C 88, 024901 (2013).
- [40] Y. Zhong, C. B. Yang, X. Cai and S. Q. Feng, Advances in High Energy Physics, 2014, 193039 (2014).